The Effect of Pressurization Rate and Pattern on Injection- Induced Seismicity in Highly Permeable Sandstone

An Experimental Study

Naderloo, M.; Veltmeijer, A.; Pluymakers, A.; Jansen, J.D.; Barnhoorn, A.

DOI
10.1029/2024JB029469

Publication date
2025

Document Version
Final published version

Published in
JGR Solid Earth

Citation (APA)
Naderloo, M., Veltmeijer, A., Pluymakers, A., Jansen, J. D., & Barnhoorn, A. (2025). The Effect of Pressurization Rate and Pattern on Injection- Induced Seismicity in Highly Permeable Sandstone: An Experimental Study. *JGR Solid Earth*, *130*(12), Article e2024JB029469. https://doi.org/10.1029/2024JB029469

JGR Solid Earth

RESEARCH ARTICLE
10.1029/2024JB029469

Special Collection:
Solid Earth Geophysics as a means to address issues of global change

The Effect of Pressurization Rate and Pattern on Injection-Induced Seismicity in Highly Permeable Sandstone: An Experimental Study

M. Naderloo[1], A. Veltmeijer[1], A. Pluymakers[1], J. D. Jansen[1], and A. Barnhoorn[1]

[1]Department of Geoscience and Engineering, Delft University of Technology, Delft, The Netherlands

Key Points:

- Laboratory investigation of the effect of pressurization rate and pattern on fault slip behavior
- A high pressurization rate may lead to a sudden decrease in effective normal stress, resulting in elevated slip velocity
- A cyclic recursive pattern in faulted, highly permeable sandstone resulted in more frequent and abrupt slow slip events

Supporting Information:

Supporting Information may be found in the online version of this article.

Correspondence to:

M. Naderloo,
m.naderloo@tudelft.nl

Citation:

Naderloo, M., Veltmeijer, A., Pluymakers, A., Jansen, J. D., & Barnhoorn, A. (2025). The effect of pressurization rate and pattern on injection-induced seismicity in highly permeable sandstone: An experimental study. *Journal of Geophysical Research: Solid Earth*, *130*, e2024JB029469. https://doi.org/10.1029/2024JB029469

Received 5 MAY 2024
Accepted 1 NOV 2025

Author Contributions:

Conceptualization: M. Naderloo, A. Pluymakers, J. D. Jansen, A. Barnhoorn
Data curation: M. Naderloo
Formal analysis: M. Naderloo
Funding acquisition: J. D. Jansen, A. Barnhoorn
Investigation: M. Naderloo
Methodology: M. Naderloo, A. Veltmeijer, A. Pluymakers, J. D. Jansen, A. Barnhoorn

Abstract Effectively mitigating induced seismicity in subsurface engineering operations within highly permeable, porous geo-energy reservoirs requires a clear understanding of how fluid injection parameters influence the seismic response. In this study, we performed injection-driven fault reactivation experiments on highly permeable saw-cut Red Felser sandstone to provide new insight into the effect of injection pattern and rate on fault slip behavior and seismicity evolution. Three different pressurization rates were applied: high, medium, and low rates of 2, 1, and 0.2 MPa/min, respectively. Three injection patterns were also used: cyclic recursive, monotonic, and stepwise injections. Our results reveal that a high pressurization rate leads to increased slip velocity, more microseismic events, higher total acoustic emission (AE) energy, and a lower b-value compared to tests with low pressurization rates. We postulate that a high pressurization rate enhances the likelihood of a sudden reduction in effective normal stress, leading to fault opening and the disruption of asperity contacts. Furthermore, results from samples subjected to various injection patterns demonstrate that the cyclic recursive pattern exhibits a higher maximum slip velocity, more episodes of slow slip, and greater radiated AE energy than a monotonic pattern. In the case of the cyclic recursive pattern, increasing the number of cycles increases shear stress drop, shear slip, and maximum slip velocity. Our findings suggest that using a monotonic injection pattern and low pressurization rate may mitigate seismicity on pre-existing faults in a highly permeable, porous reservoir.

Plain Language Summary Human activities involving subsurface fluid injection projects, such as geothermal energy recovery and/or gas storage (CO_2, H_2 or methane), are widely acknowledged to cause earthquakes occasionally. This is a cause for public concern. Although several studies demonstrate that injection patterns and rates can play an essential role, the underlying physical mechanisms responsible for induced earthquakes still need to be better understood. Therefore, we performed laboratory tests on highly permeable Red Felser sandstone containing a simulated geological fault. We pumped water from the bottom of the sample using different pressurization rates and patterns while monitoring the effects on fault movement behavior. Our results showed that faster fluid injections tend to cause more rapid fault slips and generate more laboratory micro-earthquakes compared to slow injections. Among the injection patterns, the cyclic injection pattern resulted in the highest slip velocity and higher earthquake activity, indicating that the pattern of injection can impact fault movement. Our results can help improve the design of fluid injection projects to minimize the risk of inducing small earthquakes, especially in areas with pre-existing geological faults.

1. Introduction

Many human activities related to the subsurface, such as geothermal projects, water waste injection, and gas production or storage, involve the injection of pressurized fluids into the subsurface. The injection of pressurized fluids into underground formations can induce seismicity by reactivating pre-existing faults, which sometimes includes large-magnitude earthquakes (Deichmann & Giardini, 2009; Ellsworth, 2013; Ji, Yoon, et al., 2021; Ji, Zhuang, et al., 2021). Three well-known examples of induced seismicity are (a) Pohang, South Korea with a moment magnitude of 5.4 caused by a geothermal energy project (Kim et al., 2018), (b) Oklahoma, US, a magnitude 5.7 earthquake due to the waste-water injection (Keranen & Weingarten, 2018), and three events above the magnitude 3 in Basel, Switzerland during an Enhanced Geothermal Systems (EGS) project (Bachmann et al., 2012). From a physical perspective, reactivating pre-existing faults relies on the interplay of effective stress and the failure criterion. Elevating the fluid pressure diminishes the effective normal stress acting on the fault

Project administration: J. D. Jansen, A. Barnhoorn
Software: M. Naderloo, A. Veltmeijer
Supervision: A. Pluymakers, J. D. Jansen, A. Barnhoorn
Validation: M. Naderloo, A. Barnhoorn
Visualization: M. Naderloo, A. Veltmeijer, A. Pluymakers
Writing – original draft: M. Naderloo, A. Veltmeijer, A. Pluymakers, A. Barnhoorn
Writing – review & editing: M. Naderloo, A. Veltmeijer, A. Pluymakers, J. D. Jansen, A. Barnhoorn

plane. Consequently, the shear resistance decreases, enabling movement under tectonic shear stresses in natural settings (Ellsworth, 2013; Keranen & Weingarten, 2018; Nicol et al., 2011; Zang et al., 2014; Zoback & Gorelick, 2012). Mitigating and managing seismic hazards caused by injection operations with the uninterrupted functioning of geo-storage operations is essential for society. Comprehending the key factors influencing injection-induced seismicity can contribute to improving management and mitigation strategies. Several attempts have been conducted to mitigate and reduce injection-induced seismicity on laboratory and field scales (Bommer et al., 2015; Hofmann et al., 2018; Ji, Yoon, et al., 2021; Ji, Zhuang, et al., 2021; Naderloo et al., 2022). There are two injection-production related critical factors influencing seismicity. The first is the rate at which fluid pressure is increased during injection and second, the pattern of fluid injection.

To first consider the effect of fluid pressurization rate: lowering fluid pressurization rates has been shown to lead to reduced seismic hazard (Alghannam & Juanes, 2020; Ciardo & Rinaldi, 2022; French et al., 2016; Ji et al., 2022; Passelègue et al., 2018; Wang et al., 2020). High pressurization rates during experiments performed on a saw-cut Westerly granite sample (extremely low permeable) under triaxial stress conditions facilitated the transition from drained to locally undrained conditions (Passelègue et al., 2018). High pressurization rates create local fluid pressure perturbations (heterogeneous distribution of fluid pressure) capable of reactivating faults (Passelègue et al., 2018). The same phenomenon occurred with stepwise increasing fluid pressure into faulted granite samples with different roughness (Rutter & Hackston, 2017; Ye & Ghassemi, 2018) conducted triaxial shear experiments on both permeable and impermeable sandstones with a saw-cut fracture, revealing that sudden fluid pressurization can readily induce seismogenic fault slip in low-permeable rock. Conversely, in permeable sandstone rock, fluid can permeate the fault plane through the rock matrix, following the law of effective stress, and this can lead to aseismic fault sliding (Rutter & Hackston, 2017). Therefore, in low permeable rocks, localized fluid overpressures due to the high pressurization rates can initiate episodes of quasi-static, partial fault slip, which can then progress to the nucleation and propagation of earthquakes. While several studies have explored the mechanism of fault reactivation with different pressurization rates on impermeable rocks, few studies have been allocated to reveal fundamental physical mechanisms linking the rate of fluid injection to induced earthquakes in permeable rocks (Alghannam & Juanes, 2020; Ji et al., 2022; Passelègue et al., 2018; Rutter & Hackston, 2017; Ye & Ghassemi, 2018, 2020), despite the fact that many gas and/or wastewater storage sites and geothermal reservoirs are located in porous formations. The main result to date is by Wang et al. (2020) who conducted injection-induced fault slip experiments on highly permeable saw-cut sandstone using both high and low fluid pressurization rates. Their findings indicate that slip behavior is governed primarily by the pressurization rate rather than the absolute injection pressure. They demonstrated that rapid fluid injection promotes slow stick-slip behavior, whereas slower injection rates tend to result in stable fault creep. A systematic experimental study that investigates whether—and how—different pressurization rates, by altering the stress path (i.e., effective normal and shear stress), influence fault slip behavior is still lacking. As subsurface use increases—particularly in permeable reservoirs—understanding how slip behavior affects the evolution of microseismicity becomes increasingly urgent.

Second, in both intact and faulted rock, it has been shown that differences in the occurrence and distribution of induced seismicity exist between constant (monotonic) injection and injection following a pre-defined pattern, in both high- and low-permeability reservoirs. Studies on either intact specimen (sandstone and granite) (Naderloo et al., 2023; Veltmeijer et al., 2024; Zang et al., 2019; Zhuang et al., 2020) or faulted granite samples (Ji, Yoon, et al., 2021; Ji, Zhuang, et al., 2021) suggest that the seismic response to cyclic fluid injection differs from that of Monotonic Injection (MI), with cyclic injection potentially leading to reduced levels of induced seismicity (Ji, Yoon, et al., 2021; Ji, Zhuang, et al., 2021; Naderloo et al., 2023; Niemz et al., 2020; Zang et al., 2019; Zhu et al., 2021; Zhuang et al., 2020). In other words, cyclic injection provides a potential mechanism to replace the big magnitude events with many small ones (Ji, Zhuang, et al., 2021). conducted an injection-induced fault reactivation test on a critically stressed natural fracture in granite to investigate the slip behavior under cyclic and MI patterns (Ji, Yoon, et al., 2021; Ji, Zhuang, et al., 2021). When cyclic injection is conducted with a limited peak injection pressure, it induces aseismic fracture slip at significantly lower peak slip rates compared to those observed during the MI. The more uniform reduction in effective normal stress caused by cyclic injection promotes gradual and stable fracture slip, characterized by smaller peak slip rates (Ji, Zhuang, et al., 2021). Cyclic fluid injection facilitates the diffusion of fluid pressure along faults due to the sequence of fluid flowback and re-injection. Yet, the decrease in seismic moment release hinges on various cycle-related elements, including the critical injection pressure and injection frequency (Ji, Yoon, et al., 2021). Oscillating fluid pressure during fault

reactivation experiments on permeable sandstone promotes seismic behavior rather than aseismic slip. This was interpreted to be due to the alterations in critical stiffness of the fault plane (Noël et al., 2019). The conflicting conclusions drawn regarding the effectiveness of cyclic injection primarily stem from the influence of the variations in fault drainage properties and different boundary conditions (Ji, Yoon, et al., 2021; Ji, Zhuang, et al., 2021; Noël et al., 2019). Therefore, it is essential to investigate and compare the effects of different injection patterns under the same boundary conditions on a simulated fault in permeable rock.

The aim of this study is twofold: first, to investigate the effect of pressurization rates, and second, to examine the impact of injection patterns on fault reactivation mechanisms in permeable, faulted rock. This is achieved by analyzing specific seismicity parameters, including radiated acoustic emission (AE) energy, the total number of generated events, and the magnitude–frequency distribution of these events. To this end, we conduct injection-driven fault reactivation experiments on saw-cut permeable Red Felser sandstones under three different pressurization rates (high, medium, low) and using three different patterns (monotonic, stepwise, and cyclic recursive injection (CRI) patterns) whilst monitoring the fault slip and microseismic (MS) activities. Our results indicate that monotonic fluid injection and low pressurization rates reduce the likelihood of slip nucleation and associated acoustic energy release, potentially mitigating induced seismicity in highly permeable and porous media.

2. Materials and Methods

2.1. Sample Preparation

A high-porosity Red Felser sandstone was selected as the reservoir rock for the injection-driven fault reactivation experiments. This particular sandstone was collected from a quarry in the vicinity of Kaiserslautern, Germany. Cylindrical samples were drilled with a diameter of 30 mm and cut to a nominal length of approximately 75 ± 0.8 mm. The average density and porosity of the samples were determined to be 2.1 ± 0.015 g/cm3 and 21.14 ± 0.7%, respectively, using a gas expansion (helium) pycnometer. Only those with porosity falling within the range of the average porosity ±1% standard deviation were selected to minimize experimental variability.

Furthermore, all samples were cut at a 30° angle relative to the vertical cylinder axis to simulate a fault plane. The saw-cut surfaces were carefully cleaned with a soft fabric to ensure removing leftover particles and grains due to the saw cut (see Figure S1 in Supporting Information S1). Red Felser sandstone is mainly composed of quartz minerals (89.5%). To characterize the mechanical properties of Red Felser sandstone, five uniaxial compression tests were performed. The Red Felser sandstone has a UCS strength of 46 ± 3 MPa and a Young's Modulus of 16 ± 1.5 GPa. The permeability of the saw-cut sample was assessed (with respect to water) using the steady-state Darcy flow method at a confining pressure of 21 MPa, resulting in an approximate permeability of ∼1.5 Darcy. This implies that the estimated diffusion time, t_c, is less than 1.6×1^{-3} seconds (as detailed in Text S2 in Supporting Information S1). This short diffusion time, coupled with the timescale of the experiments and pore pressure buildup, indicates a homogeneous and constant pore pressure distribution. Pore fluid ramps are on the order 0.2–2 MPa/min, therefore fluid pressure throughout the sample is considered to be always at equilibrium. It is worth noting that the storage capacity—including both matrix porosity and the fault plane—was assumed to be consistent across all samples, as they were selected based on similar porosity and fabricated with identical saw-cut geometry. Additionally, the total system volume (including pumps, lines, pistons, and sample chamber) was kept identical across all tests to ensure comparability.

2.2. Testing Apparatus

For the triaxial fault reactivation tests, an instrumented Hoek cell was utilized, capable of applying confining pressure ($\sigma_2 = \sigma_3$) up to a maximum of 70 MPa. This cell was positioned beneath a uniaxial servo-control loading machine with a maximum capacity of 500 kN and a resolution of ±0.1 kN to provide the axial stress (σ_1) (see Figure 1). To isolate the rock sample and prevent interference from the confining oil, we employed a silicon jacket. Within this jacket, we embedded eight resonant-type piezoelectric transducers, each with a resonant frequency of 2 MHz, a diameter of 5 mm, and a thickness of 1 mm, making direct contact with the rock surface. These transducers recorded microseismicity or AE signals (AE was used in the laboratory as a proxy for microseismic activity observed in the field). To amplify these signals, we utilized pre-amplifiers (with a gain set to 40 dB) connected to a Richter system, which is a continuous data acquisition system (see Figure 1). The Richter system is a multi-channel setup with 16-bit ADC resolution, comprising four units that can be synchronized. Using the ExStream software, we recorded continuous waveforms at a 2 MHz sampling rate while maintaining an

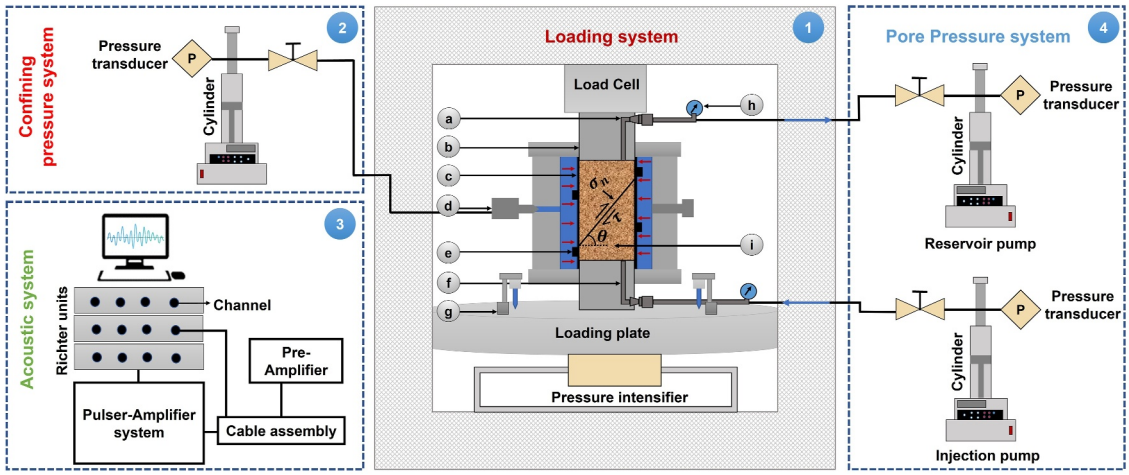

Figure 1. Schematic of the experimental setup including different units: (1) Loading system (a) outlet fluid line, (b) loading piston, (c) silicon jacket, (d) confining oil inlet, (e) acoustic emission sensor, (f) inlet fluid line, (g) linear variable differential transformer for measuring axial deformation, (h) pressure sensor, (i) saw-cut sandstone, (2) Confining pressure system, (3) Acoustic system, and (4) Pore pressure system. Note that this figure is for illustrative purposes only and does not represent the actual scale or proportions of the components.

input impedance of 50 Ω. We processed and managed the captured raw data or continuous waveforms using Insite Seismic Processor software. A trigger logic was employed to convert the continuous waveform data into single waveforms for further analysis. Regarding background noise, number of sensors (eight sensors used), and array distribution, an event was recorded if three or more transducers exceeded a voltage threshold of approximately 0.07 V within a time window of 480 μs, with a sampling rate of 2 MHz.

The axial displacement (L) was measured by averaging the readings from two linear variable differential transformers (LVDTs) positioned on the surface of the loading plate adjacent to the Hoek cell with a precision of ±1 μm and a 2 mm range (Figure 1). ISCO model 100 DM pumps were used for the pore fluid injection and confining pressure systems, which have a precision of 0.5% in reading pressure. The pore pressure system utilizes distilled water, while the confining pressure system operates with silicon oil. Pore pressure was introduced into the sample from the bottom end by the injection pump, while the top end was linked to the reservoir pump. This setup created a drained boundary condition, as illustrated in Figure 1.

2.3. Experimental Procedure

Before conducting the tests, the samples underwent complete saturation using a vacuum system located outside the loading system. Following this, saw-cut samples were meticulously positioned within the instrumented Hoek cell, and after applying 0.5 MPa of confining pressure, they were integrated into the loading system. Once the cell was integrated into the loading system, an initial 5 MPa of isostatic pressure ($\sigma_1 = \sigma_3$) was applied (stress rate was 0.05 MPa/s). Subsequently, the injection lines were flushed to eliminate air from the system. With this primary preparation completed, the main phases of the experiments proceeded as follows (see Figure 2):

Phase 1: The axial stress and confining pressure increased hydrostatically until the desired confining pressure of 21 MPa was achieved. The experimental conditions were designed to reflect the stress regime of the Groningen gas field in the Netherlands, where horizontal stresses are approximately 30 MPa (Spiers et al., 2017). However, due to the pressure limitations of the instrumented sleeve (which houses the AE sensors), the maximum confining and pore pressures were limited to 21 and 19 MPa, respectively.

Phase 2: The pore pressure was built up until it reached 3 MPa in pressure gradient control mode (fluid was injected from the bottom of the sample at a rate of 0.5 MPa/min) as the background pore pressure. Background pore pressure refers to the initial pore fluid pressure uniformly established throughout the rock sample prior to axial loading and fault reactivation. A waiting period of 15 min followed, allowing the system to equilibrate before the next phase commenced.

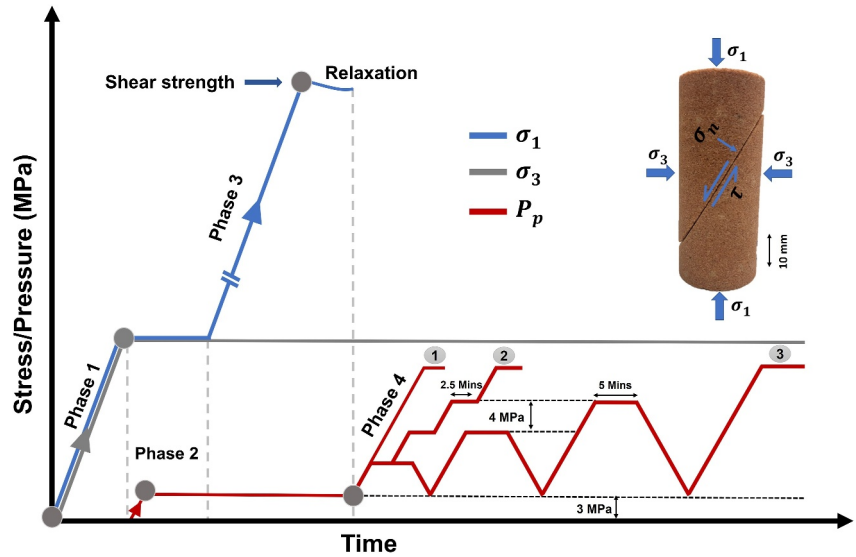

Figure 2. Schematic illustration of the experimental protocol and stress path: (1) Monotonic injection pattern, (2) Stepwise injection pattern, (3) Cyclic recursive injection pattern. The red curve indicates pore pressure (P_p), the blue curve represents axial stress (σ_1), and the gray curve denotes confining pressure (σ_3).

Phase 3: While maintaining constant pore pressure and confining pressure, the axial stress increased by continuously advancing the axial piston at a rate of 0.0005 mm/s. This process aimed to reach the shear strength through displacement-driven fault reactivation. After the fault reactivated, the axial piston was halted, and due to system relaxation, the shear stress dropped to 96% of the shear strength, resulting in a near-critically stressed condition for the fault (Wang et al., 2020; Ye & Ghassemi, 2020). After this, the test switched to a constant piston-displacement control mode, effectively locking the actuator piston. Fracture movement remained unrestricted, causing differential stress to drop significantly due to sample shortening. This means σ_1 drops without a change in σ_3. The method assumes negligible overburden deformation, allowing elastic strain energy to release during fault reactivation.

Phase 4: After reaching 96% of the shear strength, a 10-min relaxation period was implemented by holding the loading machine in constant displacement-control mode. Following this relaxation, the injection process began, involving an increase in pore pressure to induce fault reactivation through a drop in axial stress while keeping the confining pressure constant. Different injection patterns and rates were applied until the target pressure was reached. This phase allowed for the investigation of fault behavior under varying injection conditions.

During Phase 4, three different injection schemes were used in this study to investigate the effect of injection patterns on microseismicity and slip behavior, as shown in Figure 2. The first pattern, MI, involved gradually increasing the pore pressure from the background pore pressure of 3 MPa at a constant rate until reaching the target pore pressure of 19 MPa. In the second scheme, the Stepwise Injection (SI) pattern, the pore pressure was raised stepwise by 4 MPa at each step, starting from 3 MPa. There was a 5-min waiting interval between each step, continuing this process until the target pressure was achieved. Lastly, the third scheme, the CRI pattern, entailed reducing the pore pressure to 3 MPa after each cycle and increasing it by 4 MPa per cycle until reaching the final target pore pressure of 19 MPa. The waiting time in between cycles was 2.5 min (Figure 2). Notably, all injection patterns had the same pressurization rate of 2 MPa/min and reached the same final pore pressure target (19 MPa). Additionally, the MI pattern was subjected to three different pressurization rates (low, medium, and high rates, 0.2 MPa/min, 1 MPa/min, and 2 MPa/min, respectively) to explore the influence of pressurization rate on microseismicity and fault slip. Because the storage capacity was maintained constant among all samples, the injected fluid volume necessary to achieve pore pressure buildup was expected to be comparable across experiments.

2.4. Data Analysis

The shear displacement along the fault plane (δ) was calculated by total axial shortening (L_{ax}), which is calculated by excluding the contributions resulting from the elastic deformation of the test system and rock matrix (Wang et al., 2020). Thus, shear slip along the fault plane (δ) can be expressed as,

$$\delta = \frac{L_{ax}}{\cos(30)} = \frac{L_{lvdt} - \frac{F}{K_s} - \frac{F}{K_{rock}}}{\cos(30)}, \tag{1}$$

where L_{lvdt} represents the axial displacement measured by the LVDTs, and F denotes the axial force applied during the experiment. The vertical stiffness of the loading system (K_s) is 340 kN/mm, and the vertical stiffness of the sandstone matrix (K_{rock}) is 70 kN/mm. The estimation of K_s involved conducting a uniaxial compression test within elastic regime on a cylindrical aluminum dummy sample with a known elastic modulus.

The slip rate or slip velocity (v) of the fracture is defined as the first derivative of shear displacement (δ) with respect to time (t), expressed as:

$$v = \frac{d\delta}{dt}, \tag{2}$$

To determine the effective normal stress and shear stress, we employ the following equations and estimate the friction along the fault plane as the ratio between shear stress (τ) and effective normal stress (σ_n').

$$\sigma_n' = \frac{\sigma_1 + \sigma_3 - 2P_f}{2} - \frac{\sigma_1 - \sigma_3}{2}\cos(2\theta), \tag{3}$$

$$\tau = \frac{\sigma_1 - \sigma_3}{2}\sin(2\theta), \tag{4}$$

$$\mu = \frac{\tau}{\sigma_n'}, \tag{5}$$

where σ_1 and σ_3 represent the axial and confining pressure, respectively, and θ denotes the angle between the axial stress and the fault plane. Using the shear displacement (δ) the τ and σ_n values are adjusted for a changing apparent contact area of the fault plane due to fault slip (see Text S3 in Supporting Information S1) (Tembe et al., 2010). The effective normal stress is then determined by subtracting the pore pressure (P_f) from the corrected normal stress, under the assumption that the Biot coefficient is equal to 1.

To investigate microseismicity evolution, different AE parameters such as AE energy (seismic radiated energy), number of events, and b-value (magnitude-frequency distribution) were quantified. The energy of AE is directly proportional to the area beneath its waveform, in which electrical signals are assumed to have energy proportional to the square of their voltage (Equation 6) (Grosse & Ohtsu, 2008; Khazaei et al., 2015; Naderloo et al., 2019).

$$E_i = \frac{1}{R}\int_{t_0}^{t_1} V_i^2(t)\,dt, \tag{6}$$

where V_i represents the voltage of each trace point that surpasses the threshold amplitude, t_0 and t_i denote the start and end times of the transient voltage record, respectively, while R signifies the input impedance of the AE system, equal to 50 Ω.

The Gutenberg-Richter relationship describes the statistical relationship between the occurrence frequency of earthquakes and their magnitudes, often used in seismic hazard assessment. This concept can be expressed or measured in terms of a magnitude-frequency relationship (Gutenberg & Richter, 1944; Lombardi, 2003).

$$\log_{10} N = a - bM_l, \tag{7}$$

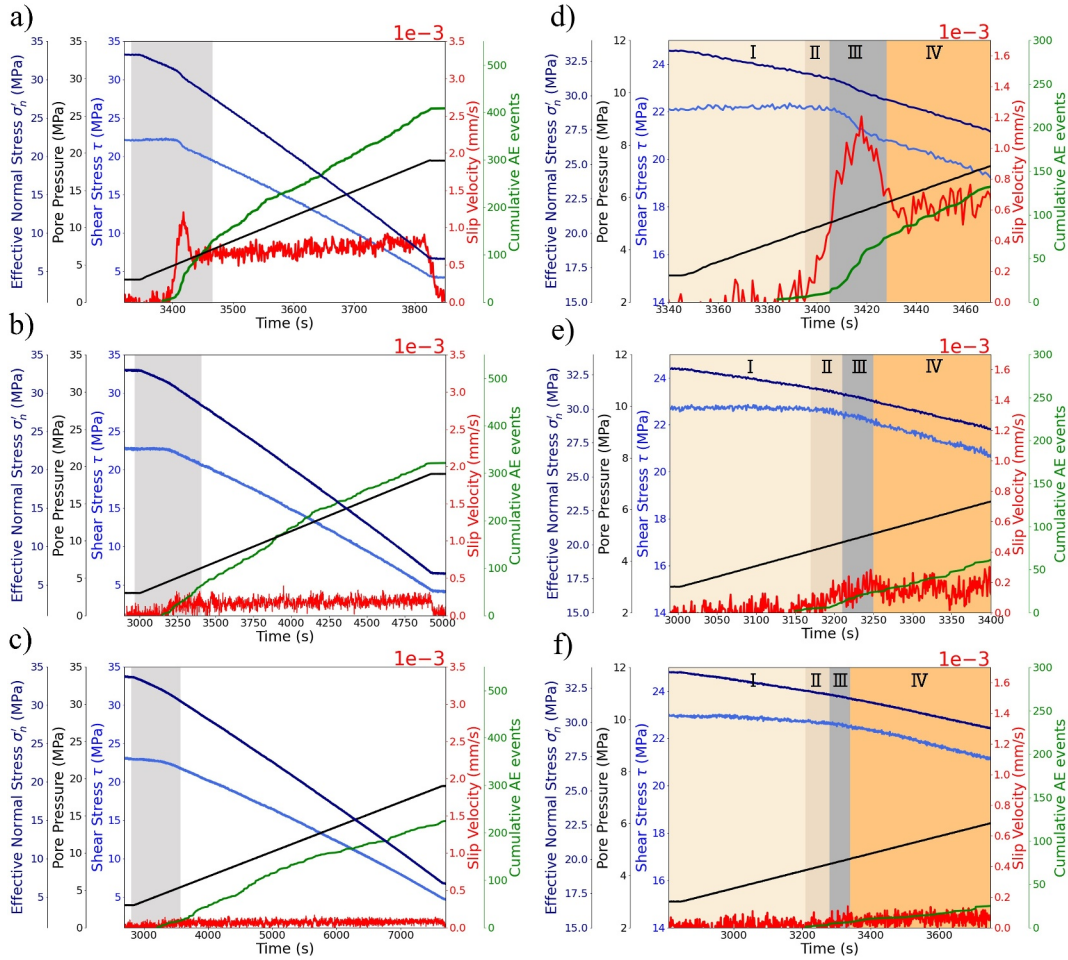

Figure 3. Temporal evolution of shear stress, effective normal stress, microseismicity, and slip velocity with increasing pore pressure (injection) in tests with different pressurization rates, (a) high rate, (b) medium rate, and (c) low rate (d, e, and f) show a zoomed-in view of the shaded area in (a, b, and c), respectively. The stages I–IV represent the onset of an increase in pore pressure, the initiation of fault reactivation accompanied by an increase in slip velocity, the subsequent increase of slip velocity reaching a peak and then declining (slow slip), and continuous sliding, respectively.

where N is the number of events with a magnitude larger than or equal to M_l, and a and b are empirical constants. The b-value represents the inverse of the slope in the logarithmic frequency-magnitude graph. A higher b-value indicates a higher proportion of small events than larger ones, a favorable characteristic for mitigating seismic activity (Lei et al., 2018). In this study, under consistent conditions across all experiments, b-value estimations are based on relative magnitudes, determined from the maximum amplitude of each event, rather than the actual AE magnitude (see Text S5 in Supporting Information S1).

3. Results

3.1. Effect of Pressurization Rate

Figures 3a–3c illustrate the results of three different pressurization rates (high, medium, and low), showcasing the temporal variations in shear stress, effective normal stress, slip velocity, and cumulative microseismic (MS) events following the injection or pore pressure increase. The shear stress was stabilized during the relaxation period prior to the start of injection at approximately 22.5 ± 0.5 MPa for all experiments. The shear stress decreases as the slip velocity increases and fault reactivation begins, as indicated by the brown zone (stage II) in Figures 3d–3f. Pore pressure values for reactivation are very similar for all pressurization rates (4.8, 4.5, and 4.1 MPa for high, medium, and low pressurization rates). This suggests that the initiation of fault reactivation is

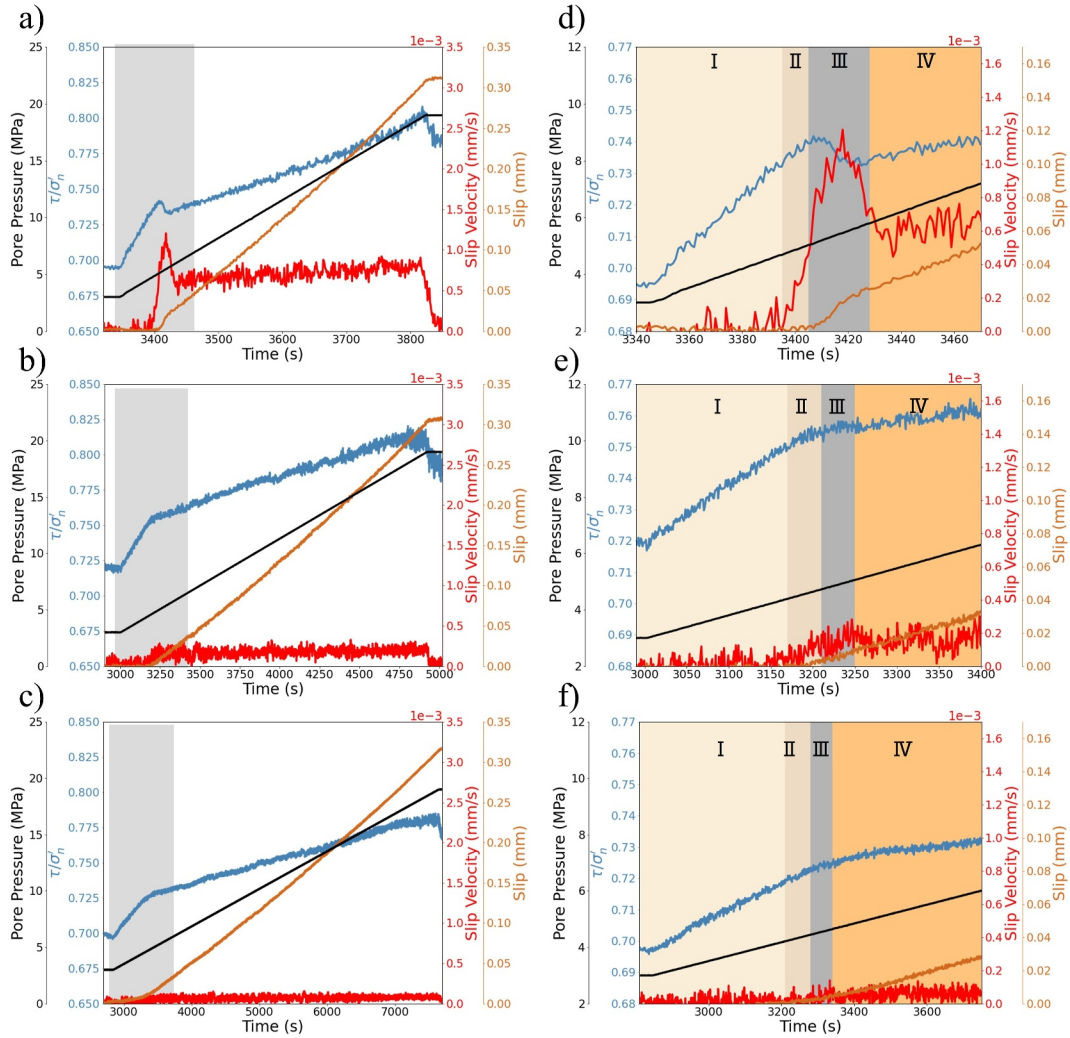

Figure 4. Evolution of friction expressed as (τ/σ_n'), shear slip, and slip velocity with building pore pressure (injection) in tests with different pressurization rates, (a) high rate, (b) medium rate, and (c) low rate. (d and e, and f) show the zoomed view of shaded area in panels (a–c), respectively.

mostly governed by the magnitude of pore fluid rather than the pressurization rate. Additionally, microseismic events are observed to commence when fault reactivation starts.

In the high pressurization rate scenario, fault reactivates when slip velocity begins to increase (depicted by the brown zone in Figure 3d, stage II). As injection progresses, velocity rapidly increases, culminating in a peak, and drops quickly, resembling a slow slip event (depicted by the gray zone in Figure 3d, stage III). Aseismic (creep) slip velocity for natural faults is generally less than 0.001 mm/s, and slow slip events have peak slip rates of less than 1 mm/s (Bürgmann, 2018; Leeman et al., 2016). The peak slip velocity is 0.0012 mm/s, thus can be considered as a slow slip. After a slow slip event, slip velocity maintains a consistent level and increases slightly by approaching the end of the injection operation (stage IV). Similar behavior is observed for the microseismic behavior in which event generation starts with the initiation of fault reactivation (Figure 3d brown shaded zone, stage II). There is a rapid surge in the number of MS events (stage III), followed by a continuous generation of microseismicity proportional to the pressurization rate as pore pressure increases (see Figures 3a and 3d). On the other hand, the medium and low pressurization rates exhibit a distinct pattern, with no sharp increase in microseismic activity (see Figures 3b, 3c, 3e, and 3f), and the MS events increase slowly and gradually relative to

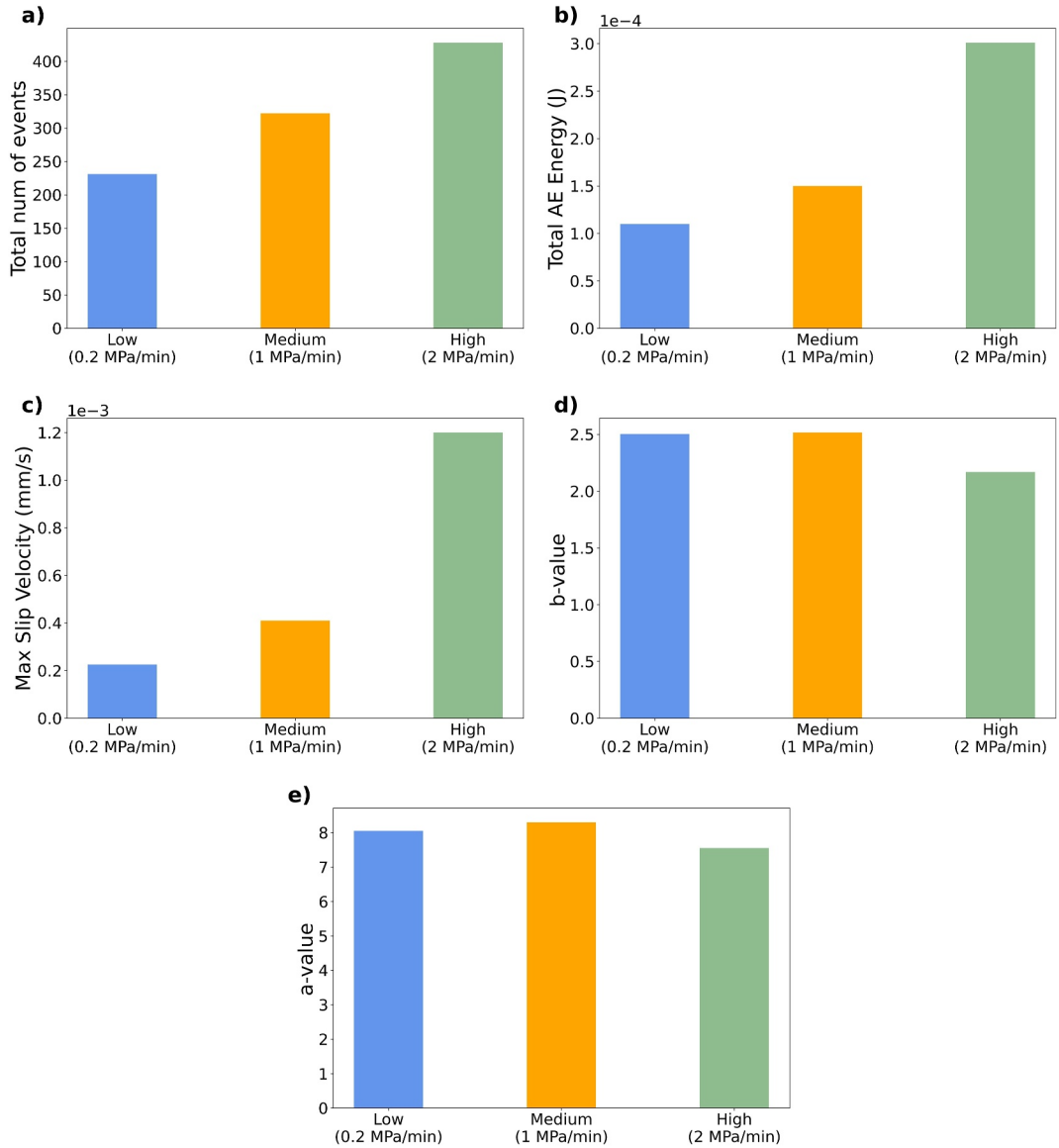

Figure 5. Comparison of different seismicity parameters obtained from experiments with different pressurization rates: (a) total number of MS events, (b) total radiated acoustic emission energy, (c) maximum slip velocity, (d) estimated b-value, and (e) estimated a-value.

their respective pressurization rates. Also, in the low-rate injection scenario, there is no slow slip (velocity acceleration and drop) during fault reactivation; instead, the slip velocity gradually increases from stage II to stage IV and fault slides (interpreted as fault creep) with a constant value as an injection or pore pressure buildup progresses. In other words the likelihood of slow slip nucleation and a drastic increase in the number of events at the onset of fault reactivation is minimized by reducing the pressurization rate. The high pressurization rate is characterized by higher maximum slip and continuous slip velocity compared to the medium and low pressurization rates.

Frictional evolution, expressed as (τ/σ_n') for all the pressurization rates is shown in Figure 4. As the injection initiates and pore pressure builds up, the friction increases linearly for all pressurization rates (Figures 4a–4c, stage I). In the case of a high pressurization rate, following the linear increase of the friction to a static friction coefficient (Figures 4a and 4d, stage II), it subsequently drops, coinciding with the maximum slip velocity and the occurrence of a slow slip event (stage III). After the friction drop, it gradually recovers and increases with the

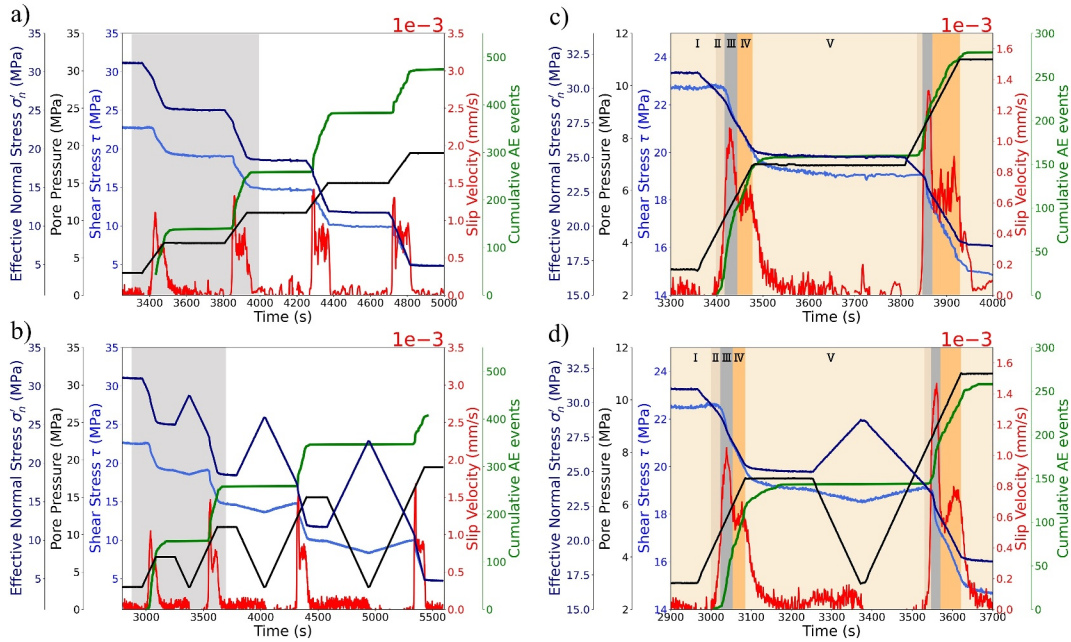

Figure 6. Temporal evolution of shear stress, effective normal stress, microseismicity, and slip velocity for stepwise injection (SI) and cyclic recursive injection (CRI) patterns. (a) SI pattern. (b) CRI pattern. (c) and (d) show a zoomed-in view of the shaded area in panels (a and b), which includes the first and second step/cycle of injection for SI and CRI patterns, respectively. The stages I–V represent the onset of an increase in pore pressure (silent area), the initiation of fault reactivation accompanied by an increase in slip velocity, the subsequent further increase of slip velocity reaching a peak and then declining (slow slip), and continuous sliding, and decline in slip velocity following by the cessation of fault slip, respectively.

further increase in pore pressure (stage IV). There is no drop in friction for the cases of medium and low pressurization rates (Figures 4b, 4c, 4e, and 4f). After slip velocities reach their constant rates (Figures 4b, 4c, 4e, and 4f), a nearly linear increase in friction is observed with a further increase in pore pressure, similar to the high pressurization rate case after the friction drop (slow slip). At the end of the injection operations (i.e., after building up 19 MPa pore pressure in the system), the total shear stress drop and total shear slip are 17.5 ± 0.3 MPa and 0.32 ± 0.005 mm, respectively, very similar for all three pressurization rates (Figures 3 and 4).

While the total shear displacement and total shear stress drop remain consistent across various pressurization rates (Figure 4), and all cases experience stable sliding, the seismicity pattern and slip velocity differ. Figure 5 directly compares the number of events (Figure 5a), total radiated AE energy (Figure 5b), maximum slip velocity (Figure 5c), and *b*-value (Figure 5d) across tests with different pressurization rates. There is a clear difference between the high pressurization rate experiments and the low or medium pressurization rate experiments. With a high pressurization rate, the radiated total AE energy, maximum slip velocity, and the total number of events, all exhibit higher values than in the other experiments. Moreover, the *b*-value is elevated in the medium and low-rate pressurization cases (Figure 5d, Text S5 and Figure S3 in Supporting Information S1). Together this suggests the high pressurization rate leads to more pronounced seismic activity and slip motion. Despite this difference in overall AE activity, the a-values derived from the Gutenberg-Richter relation are broadly comparable across all cases (Figure 5e).

3.2. Effect of Injection Pattern

Figure 6 depicts the evolution of shear stress, effective normal stress, slip velocity, and microseismic (MS) events while building up pore pressure through stepwise and cyclic recursive patterns. The data can be divided into five stages. The SI and CRI patterns share stages I–IV with the MI pattern, including stage I (silent zone based on MS activity and without fault movement), stage II (start of MS activity and reactivation with an increase in slip velocity), stage III (the further acceleration of slip velocity reaching a peak and then declining (slow slip)), and stage IV (continuous sliding) (Figure 6). However, there is another stage when injection stops or reduces between cycles in which MS activity remains absent, and slip velocity approaches near-zero values (stage V). To focus first

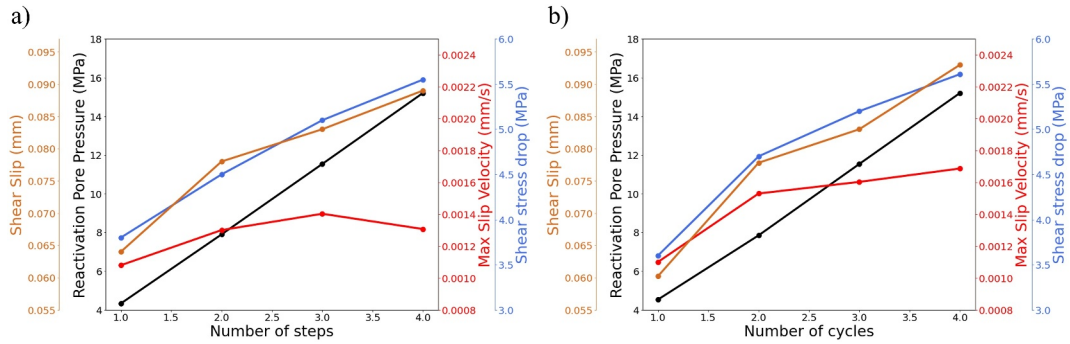

Figure 7. Evolution of key mechanical parameters over four pressurization cycles/steps. (a) Stepwise injection injection pattern and (b) Cyclic recursive injection pattern. Both panels show the progression of reactivation pore pressure (green), shear slip (orange), maximum slip velocity (red), and shear stress drop (blue) with increasing number of cycles/steps.

on stage V of the SI pattern, once the pore pressure reached 7 MPa during the first step, the injection pump was halted and pressure maintained at a constant level for 5 min (see Figures 6a and 6c). Throughout this waiting period, the shear stress and effective normal stress experienced a gradual decline and stabilized, accompanied by the absence of microseismic activity (stage V in Figure 6). Additionally, the slip velocity diminished nearly to zero. Comparing that to phase V of the CRI pattern, following the first cycle, a waiting period of 2.5 min followed, sufficient for the relaxation of shear stress and MS activity cessation (Figures 6b and 6d, stage V). After waiting time, the pore pressure was reduced (depleted) to 3 MPa, serving as a reference or background pore pressure. For both SI (waiting time only) and CRI (waiting time plus time spent for pressure depletion), injection recommences to elevate the pore pressure within the system further to reach the next target (11 MPa). The MS activity shows that the fault reactivates when pore pressure is 7.9 MPa during the second cycle/step, and reactivation stages are similar to the prior step/cycle (see the colors for stages of reactivation in Figures 6c and 6d). Increasing the total number of injection cycles (CRI) or steps (SI) results in a noticeable rise in peak slip velocity, shear stress drop,

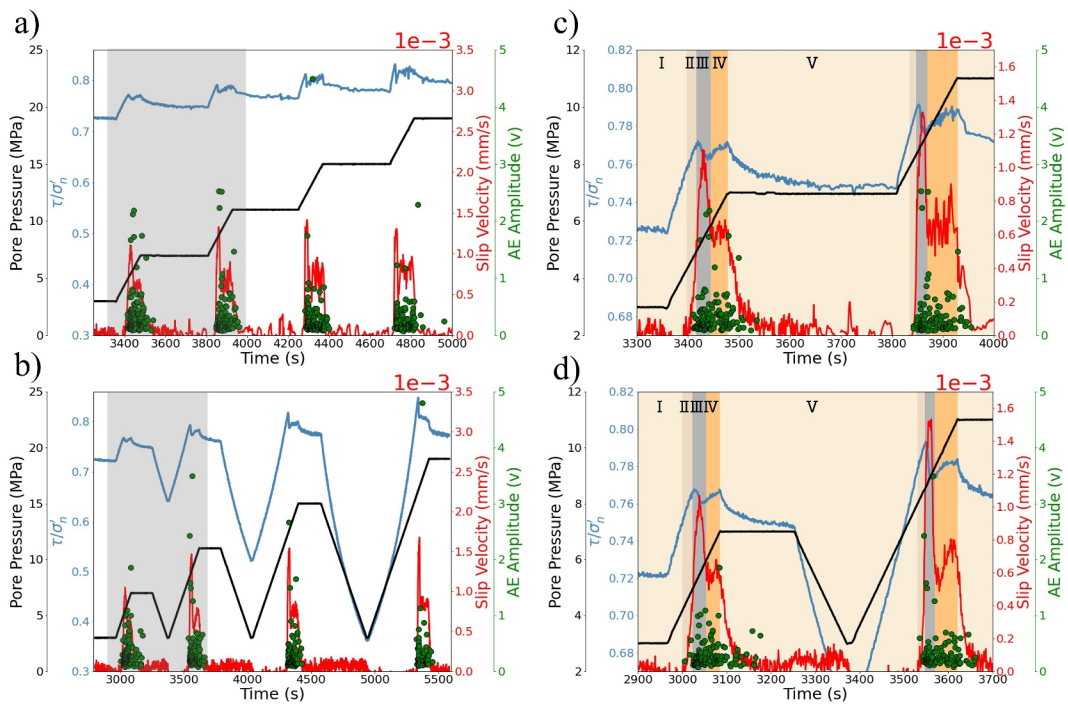

Figure 8. Evolution of τ/σ_n' (friction) with clustering of MS events per cycle/step. (a) Stepwise injection (SI) pattern. (b) Cyclic recursive injection (CRI) pattern. (c) and (d) show a zoomed view of the shaded area in panel (a) and (b), which includes the first and second step/cycle of injection for the SI and CRI patterns, respectively.

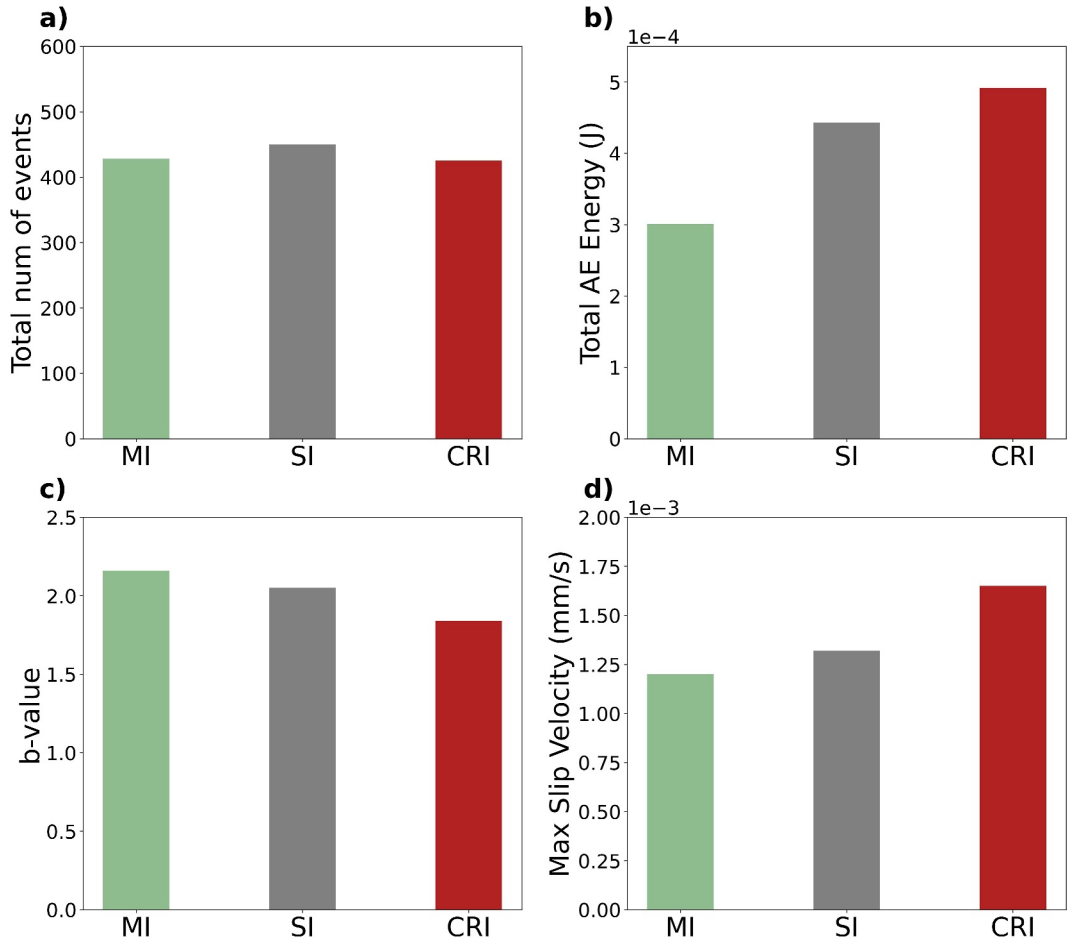

Figure 9. Comparison of different parameters obtained from the experiment with different injection patterns (monotonic injection, stepwise injection, and cyclic recursive injection): (a) total number of MS events, (b) total radiated acoustic emission energy, (c) *b*-value estimation, and (d) maximum slip velocity.

total shear slip, and reactivation pore pressure (see Figure 7). However, the increase in maximum slip velocity per step in the SI pattern is less pronounced than the increase per cycle observed in the CRI pattern.

Comparing the MI, SI, and CRI injection patterns, the evolution of shear stress and effective normal stress differs notably among the protocols (see Figures 3a, 6a and 6b). In the CRI pattern, the effective normal stress varies directly with pore pressure, increasing and decreasing in response to changes in pressure. The SI pattern, by contrast, exhibits a stepwise reduction in effective normal stress (Figures 6a and 6b). In the MI pattern, both shear stress and effective normal stress decrease continuously, corresponding to the monotonic increase in pore pressure (Figure 3a). Across all three injection protocols, differences in the evolution of shear and effective normal stress result in distinct slip behaviors. The MI leads to a single slow slip event (i.e., a slow stick-slip), while the SI and CRI patterns give rise to episodic slow slip events, with one occurring in each step or cycle.

Figures 8a and 8b further investigate the evolution and correlation of friction and AE amplitudes with pore pressure changes for SI and CRI patterns. Throughout the course of the experiment, there is a semi-continuous increasing trend in friction (Figures 8c and 8d). In stages I and II, with increasing pore pressure in each cycle/step, a slight and almost immediate increase is observed for friction of ~0.045 (it is detailed in Text S4 in Supporting Information S1). In stage III, once reactivation starts, the friction drops, concurrent with a sharp increase in slip velocity. In stage IV, friction recovers and starts to increase again as the pore pressure further increases until injection stops for that cycle or step. Each step or cycle comes with a cluster of microseismic (MS) events during injection (depicted in Figures 8c and 8d), and the amplitude of the events increases during each successive step/cycle. In the case of the CRI pattern, the Kaiser effect was observed, such that microseismic (MS)

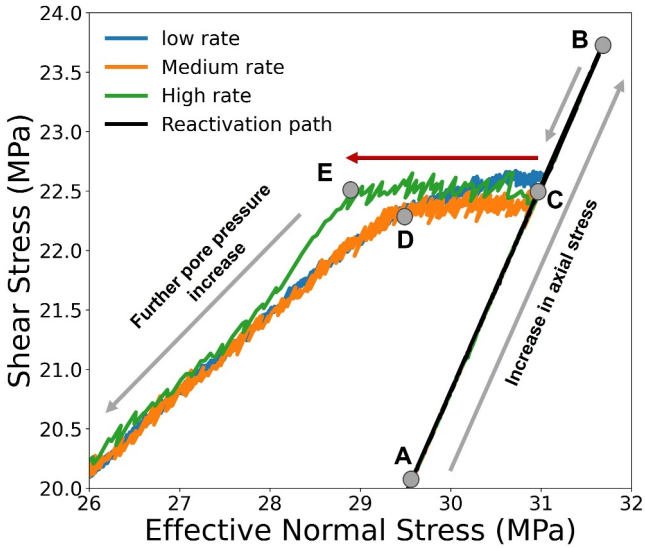

Figure 10. Stress path for different pressurization rates. The black line shows displacement-driven fault reactivation (from point A to B, axial stress increase) and the following relaxation before injection starts (from point B to C). Pore pressure buildup starts from point C and changes the stress path by changing shear and effective normal stress. During the highest pressurization rate, the effective normal stress drops by approximately 2.1 MPa within 45 s (from point C to E). For the medium pressurization rate, this drop takes approximately 100 s for a 1.5 MPa reduction to occur (from point C to D). For the low pressurization rate, there is no sudden drop in effective normal stress; instead, it gradually decreases along with shear stress as pore pressure increases.

activity remained absent during depressurization and upon subsequent re-pressurization (see Figure S6 in Supporting Information S1 for details). However, since the pore pressure required for reactivation increases with each cycle (Figure 7b), MS events do not occur immediately upon reaching the previous cycle's maximum pore pressure. This increase in reactivation pressure is attributed to a reduction in axial deviatoric stress—carried over from the preceding cycle—which renders the system less critically stressed. As a result, MS events are only triggered at higher injection pressures.

Similar to comparison presented in Figure 5 for experiments conducted at various pressurization rates, Figure 9 compares the total number of MS events, total radiated AE energy, maximum slip velocity, and estimated b-value across different injection patterns. There is no significant discrepancy in the total number of generated events (Figure 9a). However, it is noteworthy that the maximum slip velocity and the total radiated AE energy resulting from the CRI pattern surpass those of the MI and SI patterns. This observation indicates that the larger events generated during the CRI pattern may be attributed to the higher slip velocity resulting from abrupt shear stress drops. Furthermore, the same interpretation can be drawn from b-value estimation, which reveals that using the CRI pattern decreases the b-value by 15% compared to the MI pattern (Figure 9c). This implies a relatively more significant occurrence of larger seismic events than small ones when employing the CRI pattern. Consequently, it suggests that the CRI pattern leads to more prominent seismic activity and fast slip motion in comparison to the SI and MI patterns.

4. Discussion

Over the past few years, there has been a growing interest in fine-tuning injection operations for a range of applications, including geothermal projects, hydraulic fracturing, and temporal energy storage endeavors (Patel et al., 2017; Zang et al., 2013). This increased attention is driven by the desire to minimize induced seismicity and implement effective seismic risk management. Our results show different behavior in seismicity and fault slip corresponding to different pressurization rates and patterns, providing potential input to adjust injection operations and traffic light systems for subsurface-related projects.

4.1. Destabilizing Effect of High Pressurization Rates in Faulted Permeable Rocks

Studies into the effects of fluid pressure change on fault reactivation in impermeable rocks demonstrate that localized fluid overpressures (where the pressure locally exceeds what is anticipated based on a uniform Coulomb criterion) can instigate periods of quasi-static or partial fault slip (Huang et al., 2021; Labuz & Zang, 2012; Passelègue et al., 2018; Viesca & Rice, 2012). Subsequently, this may be followed by earthquake nucleation and propagation, extending well beyond the initially pressurized region (Rutter & Hackston, 2017). High pressurization rates can increase the chance of localized fluid overpressures and slip nucleation (Passelègue et al., 2018). However, in a highly permeable medium, the chance of localization of pore pressure is low due to the drainage conditions along the fault (Wang et al., 2020). showed that in the context of permeable fault structures, the mode of fault slip is predominantly influenced by the rate of fluid pressurization rather than the magnitude of pore pressure. We observed a similar result: a high pressurization rate induced a slow slip event at the beginning of fault reactivation. In contrast, with medium and low pressurization rates, fault reactivation started without the nucleation of slow slip events, and exhibited a gradual increase in slip velocity, despite the same level of pore pressure (Figure 3). Our results also demonstrate that the pressurization rate influences the seismic response—specifically, the maximum slip velocity, radiated AE energy, total number of events, and b-value (Figure 5). In particular, a lower injection rate is associated with reduced seismicity, lower AE energy release, and fewer large-magnitude MS events, as indicated by the estimated b-value.

To explain how and why the pressurization rate can influence the fault slip behavior and subsequently, seismicity response, we will discuss our results within the context of frictional models. The process of frictional evolution is

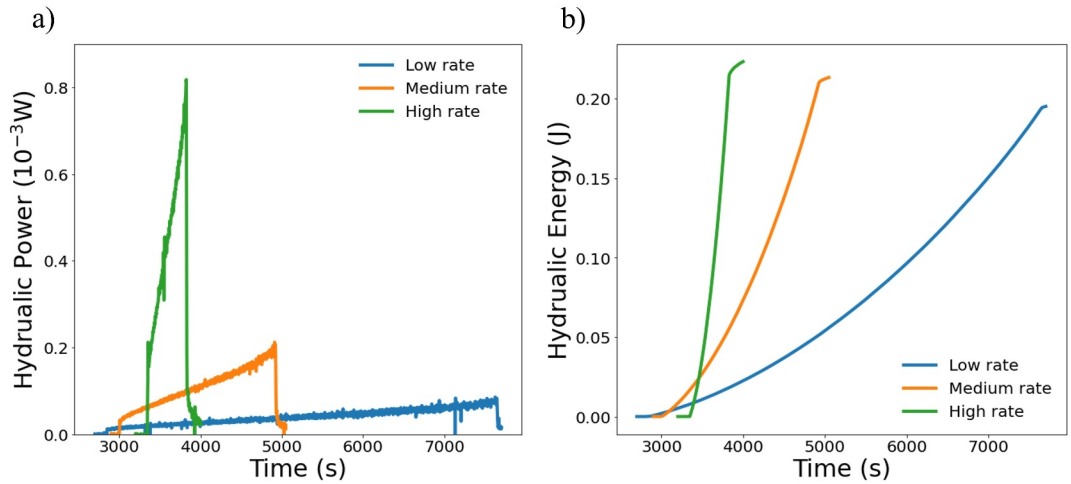

Figure 11. (a) Evolution of hydraulic power and (b) imposed total hydraulic energy into the system for the tests with different pressurization rates.

described through the utilization of rate-and-state constitutive laws, enabling the accurate replication of a diverse array of observed seismic and aseismic fault phenomena (Dieterich, 1979; Hunfeld et al., 2020; Marone, 1998; Ruina, 1983). Combining the rate-and-state friction approach with a one-dimensional spring-slider model, the critical stiffness marks the point of transition from stable to unstable slip (Dieterich, 1979; Noël et al., 2019; Rice, 1993; Ruina, 1983). As a consequence of fluid injection, there is a change in the effective normal stress (Alghannam & Juanes, 2020). adopted a one-dimensional spring-slider model as outlined by Linker and Dieterich (1992) to the poroelastic spring–slider system with an evolving pore pressure in which the critical stiffness (K_{crit}) is given by:

$$k_{crit} = \frac{(\hat{b} - \hat{a})}{d_c}\left(\sum - P\right) + \frac{\hat{a}}{V_0}\dot{P}, \tag{8}$$

where the term $\hat{b} - \hat{a}$ represents the original rate-and-state parameters (experimentally derived parameters), d_c is critical slip distance, $\sum$ is normal stress, V_0 is reference velocity, and α is a scaling factor, P is pore pressure and $\dot{P}$ is the pressurization rate.

Slip occurs through stick-slip behavior (unstable) if (a–$b < 0$) and the stiffness of the loading system (k) falls below a critical threshold ($k < k_{crit}$), while for $k > k_{crit}$, the system is linearly stable to small perturbations, leading to stable sliding. However, in the non-linear regime, frictional state evolution can influence slip stability. For the poroelastic spring–slider system, frictional instability hinges on both pore pressure magnitude and its rate of change. The influence of $\dot{P}$ prevails during the rapid early growth of pore pressure, elevating the critical stiffness. However, as pore pressure diffuses and stabilizes, P takes over, causing a decline in critical stiffness (Alghannam & Juanes, 2020; Cappa et al., 2019; Heimisson et al., 2019).

The initial destabilizing impact of the pressurization rate ($\dot{P}$) is likely linked to a transient influence on contact interlocking (Alghannam & Juanes, 2020). Figure 10 depicts changes in normal effective and shear stress due to the pore pressure increase for different pressurization rates. Notably, the high-rate injection scenario exhibits a sudden $\sim$ 2.1 MPa drop in effective normal stress (red arrow), distinct from the behavior corresponding to the medium and low-rate injection at the start of fault reactivation (Sun et al., 2024). This abrupt drop can potentially result in fault opening and the disruption of asperity contacts (Wang & Scholz, 1994), although direct measurements and observations of this are not available, leading to a phase of slow slip (Figure 3d, stages II and III). Additionally, Figure 11 presents the calculated total hydraulic energy and evolution of hydraulic power across all pressurization rates. The input power of the system, known as hydraulic power, is calculated by multiplying the injection fluid pressure (P) by the injection rate (q). By integrating hydraulic power over the injection interval, we determined the hydraulic energy involved (Goodfellow et al., 2015). Although the total hydraulic energy input

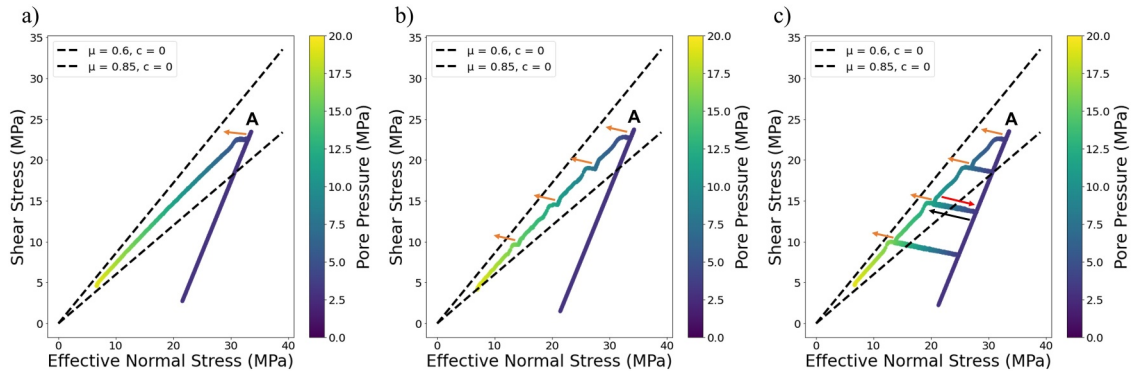

Figure 12. Illustrating the evolution of stress paths in the shear stress-effective normal stress space. Initially, up to point A, the stress path undergoes changes solely due to variations in axial stress (displacement-driven), while pore pressure and confining pressure remain constant. Following point A and the associated relaxation period, injection commences, with the color bar indicating the increasing pore pressure. The figure includes three scenarios: (a) Monotonic injection pattern, (b) Stepwise Injection pattern, and (c) Cyclic recursive injection pattern. The orange arrows indicate the moments of reactivation and stress drop, while the red and black arrows mark the depletion of pore pressure and the re-injection process.

into the system does not differ substantially—given the same injected water volume and assuming similar storage capacity for the homogeneous Red Felser sandstone—a significant contrast is observed in the magnitude of hydraulic power. Specifically, there is a noticeable surge in hydraulic power in the case of high pressurization rates (Figure 11). This rapid increase in hydraulic power may plausibly explain the sudden decrease in effective normal stress. Consequently, higher pressurization rates enhance the likelihood of a sudden reduction in effective normal stress. This sequence of events can ultimately trigger slow slip and contribute to the occurrence of high-energy microseismic events.

4.2. Stabilizing Effect of Pore Pressure in Permeable Faulted Rocks

As mentioned in the previous section (poroelastic spring–slider system), after pore pressure diffuses and reaches a steady state, the stabilizing influence of pore pressure (P) starts by reducing the critical stiffness (Equation 8), which is more likely associated with its impact on interface locking. Elevated pore pressure reduces the effective normal stress, potentially decreasing the degree of interface locking along the fault. As a result, this reduction in locking limits the potential magnitude of stress drops during fault slip (Alghannam & Juanes, 2020; Cappa et al., 2019; Moreno et al., 2010; Segall et al., 2010) showed that fluid pressure initially induces accelerating aseismic creep and fault opening. As fluid pressure continues to increase, friction evolves toward a rate-strengthening regime, promoting stable, aseismic slip. These interpretations (stabilizing effect of pore pressure) are consistent with our findings. As shown in Figure 4, an increase in friction is observed for all pressurization rates as pore pressure builds up. This trend is also reflected in the cumulative microseismic (MS) event counts and MS event rates, which exhibit no abrupt spikes, indicating stable sliding across all cases (Figure 3).

In our idealized laboratory setup, high pressurization rates initially destabilize the fault, triggering instability due to rapid pore pressure increases, while stabilization occurs later as pore pressure diffuses and its magnitude becomes dominant. However, in real-world scenarios, heterogeneity in the rock matrix surrounding the fault and fault gouge mixtures within the fault plane can lead to a non-uniform and time-varying pore-pressure field during fluid injection. This implies that the effects of the pressurization rate (rate front, referring to the spatial propagation of pore-pressure increase) may be even more pronounced, with a prolonged influence before pore pressure diffusion allows the pressure magnitude to dominate and stabilize the fault. These observations further highlight that variations in boundary conditions—such as permeability, saturation state, and stress configuration—can strongly influence the evolution of pore pressure and fault slip behavior, emphasizing the need for continued investigation under different experimental and field scenarios.

Furthermore, it is worth noting that the calculated fault stiffness remains constant at approximately $k_f \approx 58$ MPa/mm (slope of the shear stress vs. shear slip which is shown in Figure S4 in Supporting Information S1) across all tests conducted, regardless of varying pressurization rates and patterns. The system's stiffness measures approximately 270 MPa/mm, well above the stiffness of the fault ($k > k_f$), and therefore the behavior of fault slip remains mechanically stable throughout all tests conducted with different pressurization rates. Hence, the

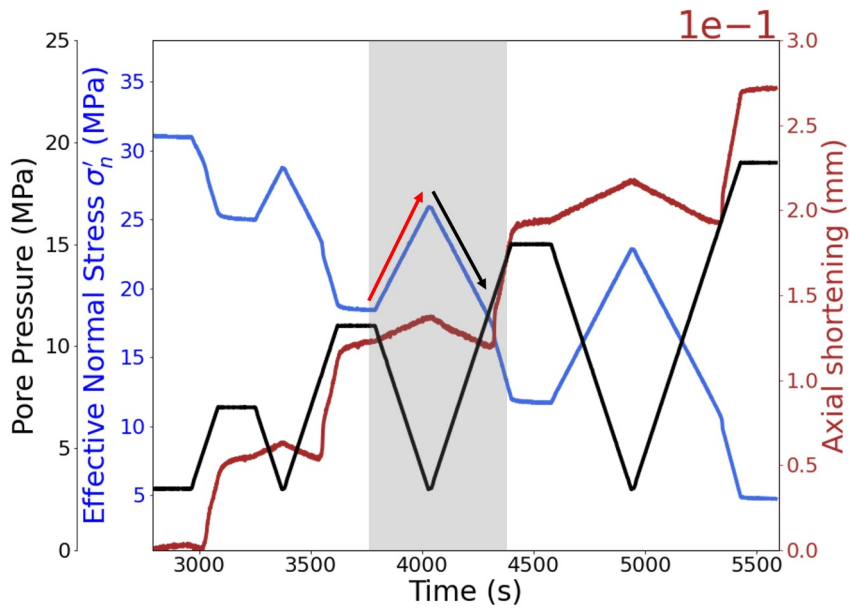

Figure 13. Change in effective normal stress and axial shortening of the sample per cycle until the end of the injection operation (Cyclic recursive injection pattern). The shaded area shows fault compaction (red arrow) and fault dilation (black arrow), indicated by increases and decreases in effective normal stress.

combined effects of pore pressure build-up and the high stiffness of the system serve to ensure stable sliding behavior across all test scenarios, even though slow stick-slip is observed in cases of high pressurization rates.

4.3. Effect of Injection Pattern on Fault Reactivation

Many investigations into seismicity in low permeable faulted or intact rock have suggested that the seismic reaction to cyclic fluid injection contrasts with that of MI, hinting at the possibility of cyclic injection resulting in diminished levels of induced seismic activity (Ji, Yoon, et al., 2021; Ji, Zhuang, et al., 2021; Naderloo et al., 2023; Niemz et al., 2020; Zang et al., 2019; Zhuang et al., 2020). Our findings reveal distinct behaviors among different injection patterns on saw-cut permeable sandstone. When using the CRI pattern, we observe the occurrence of slow slip in each cycle, whereas, in the MI pattern, slow slip nucleates only once during fault reactivation (Figures 3a and 6b). Additionally, slow slip events occur at each step of pore pressure increase in the SI pattern (Figure 6a). Notably, the CRI pattern induces a higher maximum slip velocity than MI and SI patterns (Figure 9d). Furthermore, our microseismic analysis underscores that while there is no significant difference in the total number of events generated across all three injection patterns, employing the CRI pattern generates larger magnitude events in contrast to the MI and SI patterns. This discrepancy is attributed to the higher total radiated AE energy observed in the CRI pattern (Figure 9b).

Moreover, the *b*-value extracted from the CRI pattern is lower than those of the MI and SI patterns, indicating a greater prevalence of larger-magnitude events (Figure 9c). The four slow slip events induced by the CRI pattern each exhibit a higher maximum slip velocity (Figure 6b) than the single slow slip event observed in the MI pattern (Figure 3a), as summarized in Figure 9. Intuitively, having four slip events, each with a higher peak velocity than a single lower-velocity event, would be expected to produce larger seismic events. In other words, the combination of more frequent slip episodes and higher peak slip velocities likely explains the increased microseismic activity associated with the CRI pattern.

Next, we will discuss the differences in slip behavior and seismicity resulting from the different injection patterns in terms of (1) the effect of pressure rate front (pressurization rate ($\dot{P}$)), and (2) fault compaction and dilation.

1. Figure 12 illustrates the stress path for all patterns. Specifically, at the start of each cycle or step in the CRI and SI patterns, we observe a notable and sudden drop in effective normal stress (orange arrows). Since both patterns were conducted with a high pressurization rate (2 MPa/min), the initial destabilizing influence of the

rate front ($\dot{P}$) will result in a sudden drop in effective normal stress (i.e., Figure 12). This rate front leads to fault opening and the disruption of asperity contacts and subsequently initiates a phase of slow slip (Alghannam & Juanes, 2020; Wang & Scholz, 1994). During both the SI and CRI patterns, when pore pressure stops increasing between each cycle/step, we allow the system to stabilize and reach equilibrium. Each time pore pressure rises the perturbing and destabilizing impact of the pressure rate ($\dot{P}$) comes into play.

2. In the case of CRI, by reducing the pore pressure, the effective normal stress (σ_n') exerted on the fault rises (as indicated by the red arrow in Figures 12c and 13), resulting in fault compaction. The compaction is illustrated in Figure 13, which increases sample axial shortening. The absence of any associated MS event or change in slip velocity during the reduction of the pore pressure suggests that shear slip is not occurring, and the observed behavior is attributable to fault compaction with an additional contribution from the poroelastic response of the rock matrix. The effective normal stress acting on the fault plane decreases again through elevating pore pressure (Figures 12c and 13, black arrow). The reduction in effective normal stress leads to fault dilation and a tendency for the porous rock to expand in volume during pore pressure buildup. This is evident in Figure 13, where re-injection results in a decrease in axial shortening, indicating poroelastic expansion and fault dilation. Primarily, fault compaction can enhance the likelihood of healing even in the time scale of depressurization ramp (minutes) which increases the shear strength of the quartz-rich fault plane (see Figure S1 in Supporting Information S1) (Hunfeld et al., 2017; Seyler et al., 2023). In fact, frictional healing would promote the strengthening of the fault by effectively locking it during the compaction phase (as pore pressure decreases). Consequently, overcoming the high shear strength can trigger abrupt slips. Additionally, the interplay of fault dilation and compaction through fluctuations in effective normal stress can influence and oscillate the critical stiffness of the fault shown in Equation 8 (Noël et al., 2019).

5. Conclusions

We conducted triaxial fault reactivation experiments on saw-cut Red Felser sandstones under different pressurization rates and patterns to reveal the effect of pressurization rate and pattern on microseismicity pattern and fault slip. The results show that:

1. A high pressurization rate increases the likelihood of a sudden reduction in effective normal stress, promoting the nucleation of slow slip events. In contrast, a low pressurization rate leads to a more gradual decrease in effective normal stress, reducing the propensity for slow slip nucleation.
2. A low pressurization rate is characterized by a lower maximum slip velocity, resulting in lower total radiated AE energy and a reduced total number of microseismic events. In contrast, it exhibits a higher b-value compared to a high pressurization rate.
3. A cyclic recursive pattern in highly porous and permeable sandstone resulted in more frequent and abrupt slow slip events compared to a MI pattern.
4. Shear slip, shear stress drop, and maximum slip velocity all increase progressively from the first to the fourth cycle or step during both the SI and CRI patterns.
5. Under the studied conditions, the MI pattern appears to be more effective in reducing seismicity in high-permeability sandstone compared to cyclic recursive and SI patterns.

Conflict of Interest

The authors declare no conflicts of interest relevant to this study.

Data Availability Statement

The experiments and data collection (loading data and waveforms) for this publication were conducted using the laboratory facilities at TU Delft. This data is available at https://doi.org/10.4121/02c46099-0f1e-486b-91b9-b5f0ecb30bc4.v1 or Naderloo et al. (2024).

Acknowledgments
This publication is part of the project "Science4Steer: a scientific basis for production and reinjection strategies to minimize induced seismicity in Dutch gas fields" (DEEP. NL.2018.046) of the research programme "DeepNL" which is financed by the Dutch Research Council (NWO). We would like to express our sincere gratitude to the entire technical team in the Rock Deformation Lab at Delft University of Technology.

References

Alghannam, M., & Juanes, R. (2020). Understanding rate effects in injection-induced earthquakes. *Nature Communications*, *11*(1), 3053. https://doi.org/10.1038/s41467-020-16860-y

Bachmann, C. E., Wiemer, S., Goertz-Allmann, B. P., & Woessner, J. (2012). Influence of pore-pressure on the event-size distribution of induced earthquakes. *Geophysical Research Letters*, *39*(9). https://doi.org/10.1029/2012gl051480

Bommer, J. J., Crowley, H., & Pinho, R. (2015). A risk-mitigation approach to the management of induced seismicity. *Journal of Seismology*, *19*(2), 623–646. https://doi.org/10.1007/s10950-015-9478-z

Bürgmann, R. (2018). The geophysics, geology and mechanics of slow fault slip. *Earth and Planetary Science Letters*, *495*, 112–134. https://doi.org/10.1016/j.epsl.2018.04.062

Cappa, F., Scuderi, M. M., Collettini, C., Guglielmi, Y., & Avouac, J.-P. (2019). Stabilization of fault slip by fluid injection in the laboratory and in situ. *Science Advances*, *5*(3), eaau4065. https://doi.org/10.1126/sciadv.aau4065

Ciardo, F., & Rinaldi, A. P. (2022). Impact of injection rate ramp-up on nucleation and arrest of dynamic fault slip. *Geomechanics and Geophysics for Geo-Energy and Geo-Resources*, *8*(1), 28. https://doi.org/10.1007/s40948-021-00336-4

Deichmann, N., & Giardini, D. (2009). Earthquakes induced by the stimulation of an enhanced geothermal system below Basel (Switzerland). *Seismological Research Letters*, *80*(5), 784–798. https://doi.org/10.1785/gssrl.80.5.784

Dieterich, J. H. (1979). Modeling of rock friction: 1. Experimental results and constitutive equations. *Journal of Geophysical Research*, *84*(B5), 2161–2168. https://doi.org/10.1029/jb084ib05p02161

Ellsworth, W. L. (2013). Injection-Induced earthquakes. *Science*, *341*(July), 1–8. https://doi.org/10.1126/science.1225942

French, M. E., Zhu, W., & Banker, J. (2016). Fault slip controlled by stress path and fluid pressurization rate. *Geophysical Research Letters*, *43*(9), 4330–4339. https://doi.org/10.1002/2016GL068893

Goodfellow, S. D., Nasseri, M. H. B., Maxwell, S. C., & Young, R. P. (2015). Hydraulic fracture energy budget: Insights from the laboratory. *Geophysical Research Letters*, *42*(9), 3179–3187. https://doi.org/10.1002/2015gl063093

Grosse, C. U., & Ohtsu, M. (2008). *Acoustic emission testing*. Springer Science and Business Media.

Gutenberg, B., & Richter, C. F. (1944). Frequency of earthquakes in California. *Bulletin of the Seismological Society of America*, *34*(4), 185–188. https://doi.org/10.1785/bssa0340040185

Heimisson, E. R., Dunham, E. M., & Almquist, M. (2019). Poroelastic effects destabilize mildly rate-strengthening friction to generate stable slow slip pulses. *Journal of the Mechanics and Physics of Solids*, *130*, 262–279. https://doi.org/10.1016/j.jmps.2019.06.007

Hofmann, H., Zimmermann, G., Zang, A., & Min, K. B. (2018). Cyclic soft stimulation (CSS): A new fluid injection protocol and traffic light system to mitigate seismic risks of hydraulic stimulation treatments. *Geothermal Energy*, *6*(1), 27. https://doi.org/10.1186/s40517-018-0114-3

Huang, Y., Lei, X., & Ma, S. (2021). Numerical study of the role of localized stress perturbations on fault slip: Insights for injection-induced fault reactivation. *Tectonophysics*, *819*, 229105. https://doi.org/10.1016/j.tecto.2021.229105

Hunfeld, L. B., Chen, J., Hol, S., Niemeijer, A. R., & Spiers, C. J. (2020). Healing behavior of simulated fault gouges from the Groningen gas field and implications for induced fault reactivation. *Journal of Geophysical Research: Solid Earth*, *125*(7), e2019JB018790. https://doi.org/10.1029/2019jb018790

Hunfeld, L. B., Niemeijer, A. R., & Spiers, C. J. (2017). Frictional properties of simulated fault gouges from the seismogenic Groningen gas field under in situ P–T-chemical conditions. *Journal of Geophysical Research: Solid Earth*, *122*(11), 8969–8989. https://doi.org/10.1002/2017jb014876

Ji, Y., Wang, L., Hofmann, H., Kwiatek, G., & Dresen, G. (2022). High-rate fluid injection reduces the nucleation length of laboratory earthquakes on critically stressed faults in granite. *Geophysical Research Letters*, *49*(23), e2022GL100418. https://doi.org/10.1029/2022gl100418

Ji, Y., Yoon, J. S., Zang, A., & Wu, W. (2021). Mitigation of injection-induced seismicity on undrained faults in granite using cyclic fluid injection: A laboratory study. *International Journal of Rock Mechanics and Mining Sciences*, *146*, 104881. https://doi.org/10.1016/j.ijrmms.2021.104881

Ji, Y., Zhuang, L., Wu, W., Hofmann, H., Zang, A., & Zimmermann, G. (2021). Cyclic water injection potentially mitigates seismic risks by promoting slow and stable slip of a natural fracture in granite. *Rock Mechanics and Rock Engineering*, *54*(10), 1–17. https://doi.org/10.1007/s00603-021-02438-7

Keranen, K. M., & Weingarten, M. (2018). Induced seismicity. *Annual Review of Earth and Planetary Sciences*, *46*(1), 149–174. https://doi.org/10.1146/annurev-earth-082517-010054

Khazaei, C., Hazzard, J., & Chalaturnyk, R. (2015). Damage quantification of intact rocks using acoustic emission energies recorded during uniaxial compression test and discrete element modeling. *Computers and Geotechnics*, *67*, 94–102. https://doi.org/10.1016/j.compgeo.2015.02.012

Kim, K.-H., Ree, J.-H., Kim, Y., Kim, S., Kang, S. Y., & Seo, W. (2018). Assessing whether the 2017 Mw 5.4 Pohang earthquake in South Korea was an induced event. *Science*, *360*(6392), 1007–1009. https://doi.org/10.1126/science.aat6081

Labuz, J. F., & Zang, A. (2012). Mohr–Coulomb failure criterion. *Rock Mechanics and Rock Engineering*, *45*(6), 975–979. https://doi.org/10.1007/s00603-012-0281-7

Leeman, J. R., Saffer, D. M., Scuderi, M. M., & Marone, C. (2016). Laboratory observations of slow earthquakes and the spectrum of tectonic fault slip modes. *Nature Communications*, *7*(1), 1–6. https://doi.org/10.1038/ncomms11104

Lei, X., Li, S., & Liu, L. (2018). Seismic b-value for foreshock AE events preceding repeated stick-slips of pre-cut faults in granite. *Applied Sciences*, *8*(12), 2361. https://doi.org/10.3390/app8122361

Linker, M. F., & Dieterich, J. H. (1992). Effects of variable normal stress on rock friction: Observations and constitutive equations. *Journal of Geophysical Research*, *97*(B4), 4923–4940. https://doi.org/10.1029/92jb00017

Lombardi, A. M. (2003). The maximum likelihood estimator of b-value for mainshocks. *Bulletin of the Seismological Society of America*, *93*(5), 2082–2088. https://doi.org/10.1785/0120020163

Marone, C. (1998). Laboratory-derived friction laws and their application to seismic faulting. *Annual Review of Earth and Planetary Sciences*, *26*(1), 643–696. https://doi.org/10.1146/annurev.earth.26.1.643

Moreno, M., Rosenau, M., & Oncken, O. (2010). 2010 Maule earthquake slip correlates with pre-seismic locking of Andean subduction zone. *Nature*, *467*(7312), 198–202. https://doi.org/10.1038/nature09349

Naderloo, M., Barnhoorn, A., Veltmeijer, A., Jansen, J. D., & Pluymakers, A. (2024). Data from injection-driven fault reactivation experiments on faulted sandstone [Dataset]. *4TU.ResearchData*. https://doi.org/10.4121/02c46099-0f1e-486b-91b9-b5f0ecb30bc4.v1

Naderloo, M., Moosavi, M., & Ahmadi, M. (2019). Using acoustic emission technique to monitor damage progress around joints in brittle materials. *Theoretical and Applied Fracture Mechanics*, *104*, 102368. https://doi.org/10.1016/j.tafmec.2019.102368

Naderloo, M., Veltmeijer, A., Jansen, J. D., & Barnhoorn, A. (2023). Laboratory study on the effect of stress cycling pattern and rate on seismicity evolution. *Geomechanics and Geophysics for Geo-Energy and Geo-Resources*, *9*(1), 137. https://doi.org/10.1007/s40948-023-00678-1

Naderloo, M., Veltmeijer, A., Pluymakers, A., & Barnhoorn, A. (2022). Experimental investigation of the effect of stress cycling on seismicity evolution during fault reactivation process. In *83rd EAGE Annual conference and exhibition* (Vol. 2022, pp. 1–5). EAGE Publications BV. https://doi.org/10.3997/2214-4609.202210415

Nicol, A., Carne, R., Gerstenberger, M., & Christophersen, A. (2011). Induced seismicity and its implications for CO_2 storage risk. *Energy Procedia*, *4*, 3699–3706. https://doi.org/10.1016/j.egypro.2011.02.302

Niemz, P., Cesca, S., Heimann, S., Grigoli, F., von Specht, S., Hammer, C., et al. (2020). Full-waveform-based characterization of acoustic emission activity in a mine-scale experiment: A comparison of conventional and advanced hydraulic fracturing schemes. *Geophysical Journal International*, *222*(1), 189–206. https://doi.org/10.1093/gji/ggaa127

Noël, C., Passelègue, F. X., Giorgetti, C., & Violay, M. (2019). Fault reactivation during fluid pressure oscillations: Transition from stable to unstable slip. *Journal of Geophysical Research: Solid Earth*, 940–953. https://doi.org/10.1029/2019JB018517

Passelègue, F. X., Brantut, N., & Mitchell, T. M. (2018). Fault reactivation by fluid injection: Controls from stress state and injection rate. *Geophysical Research Letters*, *45*(23), 12837–12846. https://doi.org/10.1029/2018GL080470

Patel, S. M., Sondergeld, C. H., & Rai, C. S. (2017). Laboratory studies of hydraulic fracturing by cyclic injection. *International Journal of Rock Mechanics and Mining Sciences*, *95*(March), 8–15. https://doi.org/10.1016/j.ijrmms.2017.03.008

Rice, J. R. (1993). Spatio-temporal complexity of slip on a fault. *Journal of Geophysical Research*, *98*(B6), 9885–9907. https://doi.org/10.1029/93jb00191

Ruina, A. (1983). Slip instability and state variable friction laws. *Journal of Geophysical Research*, *88*(B12), 10359–10370. https://doi.org/10.1029/jb088ib12p10359

Rutter, E., & Hackston, A. (2017). On the effective stress law for rock-on-rock frictional sliding, and fault slip triggered by means of fluid injection. *Philosophical Transactions of the Royal Society A: Mathematical, Physical and Engineering Sciences*, *375*(2103), 20160001. https://doi.org/10.1098/rsta.2016.0001

Segall, P., Rubin, A. M., Bradley, A. M., & Rice, J. R. (2010). Dilatant strengthening as a mechanism for slow slip events. *Journal of Geophysical Research*, *115*(B12). https://doi.org/10.1029/2010jb007449

Seyler, C. E., Shreedharan, S., Saffer, D. M., & Marone, C. (2023). The role of clay in limiting frictional healing in fault gouges. *Geophysical Research Letters*, *50*(20), e2023GL104984. https://doi.org/10.1029/2023gl104984

Spiers, C. J., Hangx, S. J. T., & Niemeijer, A. R. (2017). New approaches in experimental research on rock and fault behaviour in the Groningen gas field. *Netherlands Journal of Geosciences*, *96*(5), s55–s69. https://doi.org/10.1017/njg.2017.32

Sun, Z., Elsworth, D., Cui, G., Li, Y., Zhu, A., & Chen, T. (2024). Impacts of rate of change in effective stress and inertial effects on fault slip behavior: New insights into injection-induced earthquakes. *Journal of Geophysical Research: Solid Earth*, *129*(2), e2023JB027126. https://doi.org/10.1029/2023jb027126

Tembe, S., Lockner, D. A., & Wong, T. (2010). Effect of clay content and mineralogy on frictional sliding behavior of simulated gouges: Binary and ternary mixtures of quartz, illite, and montmorillonite. *Journal of Geophysical Research*, *115*(B3). https://doi.org/10.1029/2009jb006383

Veltmeijer, A., Naderloo, M., Pluymakers, A., & Barnhoorn, A. (2024). Precursory signals to injection induced fault reactivation in the laboratory using active ultrasonic monitoring methods. *Journal of Geophysical Research: Solid Earth*, *129*(2), e2023JB028505. https://doi.org/10.1029/2023jb028505

Viesca, R. C., & Rice, J. R. (2012). Nucleation of slip-weakening rupture instability in landslides by localized increase of pore pressure. *Journal of Geophysical Research*, *117*(B3). https://doi.org/10.1029/2011jb008866

Wang, L., Kwiatek, G., Rybacki, E., Bonnelye, A., Bohnhoff, M., & Dresen, G. (2020). Laboratory study on fluid-induced fault slip behavior: The role of fluid pressurization rate. *Geophysical Research Letters*, *47*(6), e2019GL086627. https://doi.org/10.1029/2019gl086627

Wang, W., & Scholz, C. H. (1994). Micromechanics of the velocity and normal stress dependence of rock friction. *Pure and Applied Geophysics*, *143*(1–3), 303–315. https://doi.org/10.1007/bf00874333

Ye, Z., & Ghassemi, A. (2020). Heterogeneous fracture slip and aseismic-seismic transition in a triaxial injection test. *Geophysical Research Letters*, *47*(14), 1–9. https://doi.org/10.1029/2020GL087739

Ye, Z., & Ghassemi, A. (2018). Injection-induced shear slip and permeability enhancement in granite fractures. *Journal of Geophysical Research: Solid Earth*, *123*(10), 9009–9032. https://doi.org/10.1029/2018jb016045

Zang, A., Oye, V., Jousset, P., Deichmann, N., Gritto, R., McGarr, A., et al. (2014). Analysis of induced seismicity in geothermal reservoirs–An overview. *Geothermics*, *52*, 6–21. https://doi.org/10.1016/j.geothermics.2014.06.005

Zang, A., Yoon, J. S., Stephansson, O., & Heidbach, O. (2013). Fatigue hydraulic fracturing by cyclic reservoir treatment enhances permeability and reduces induced seismicity. *Geophysical Journal International*, *195*(2), 1282–1287. https://doi.org/10.1093/gji/ggt301

Zang, A., Zimmermann, G., Hofmann, H., Stephansson, O., Min, K.-B., & Kim, K. Y. (2019). How to reduce fluid-injection-induced seismicity. *Rock Mechanics and Rock Engineering*, *52*(2), 475–493. https://doi.org/10.1007/s00603-018-1467-4

Zhu, J. B., Kang, J. Q., Elsworth, D., Xie, H. P., Ju, Y., & Zhao, J. (2021). Controlling induced earthquake magnitude by cycled fluid injection. *Geophysical Research Letters*, *48*(19), e2021GL092885. https://doi.org/10.1029/2021gl092885

Zhuang, L., Gyu, S., Melvin, J., Kwang, D., Kim, Y., Hofmann, H., et al. (2020). Laboratory true triaxial hydraulic fracturing of granite under six fluid injection schemes and grain - Scale fracture observations. *Rock Mechanics and Rock Engineering*, *53*(10), 4329–4344. https://doi.org/10.1007/s00603-020-02170-8

Zoback, M. D., & Gorelick, S. M. (2012). Earthquake triggering and large-scale geologic storage of carbon dioxide. *Proceedings of the National Academy of Sciences*, *109*(26), 10164–10168. https://doi.org/10.1073/pnas.1202473109